Acta Materialia 294 (2025) 121166

Contents lists available at ScienceDirect

Acta Materialia

journal homepage: www.elsevier.com/locate/actamat

Plastic deformation of $CaTiO_3$ perovskite under extreme loading

Boya Li [a], Shiteng Zhao [b], Marc A. Meyers [a,*]

[a] Program of Materials Science and Engineering, University of California, San Diego, USA
[b] Lawrence Berkeley National Laboratory, Berkeley, USA

ARTICLE INFO

Keywords:
Shock compression
$CaTiO_3$
Perovskite
Dislocation
Antiphase domain boundary
Deformation mechanism
High strain rate
Extreme condition
Shock Hugoniot
TEM
HRTEM

ABSTRACT

Perovskites are important functional materials in modern technology, with numerous applications in optoelectronics, such as solar cells and LEDs, lasers, and other fields. Importantly, the lower Earth mantle is predominantly composed of perovskite. (Mg, Fe)SiO_3 and $CaSiO_3$, two of the most abundant minerals in the Earth's mantle, are not amenable to being investigated at ambient conditions because they are not stable. $CaTiO_3$ serves as an excellent analogue. Thus, high-energy laser shock compression was employed to investigate the deformation mechanisms and mechanical behavior of [010] oriented $CaTiO_3$ under extreme pressure and temperature conditions comparable to those in the mantle, albeit at significantly higher strain rates. The shear stress generated by the 70 GPa shock stress was equal to approximately 20 GPa, assuming elasticity. This is significantly higher than the Peierls-Nabarro stress required to move dislocations, around 10 GPa. In agreement with this, transmission electron microscopy revealed the generation of profuse perpendicular dislocations in [110](001) and [$\bar{1}$10](001) slip systems. The dislocation density ranged from 15×10^{12} m^{-2} to 2×10^{12} m^{-2} within 12 μm from the shocked surface. Additionally, antiphase domain boundaries along [010] and [100] were observed under the high-pressure shock conditions. $CaTiO_3$ deforms mainly through dislocation motion due to its positive Clapeyron slope and high atomic packing factor. This study sheds light upon the plastic deformation of (Mg, Fe)SiO_3 and $CaSiO_3$, which comprise most of the lower earth mantle.

1. Introduction

The lower mantle makes up about 55% of the Earth's volume. The volume fraction of perovskite in it is estimated to be above 70% [1]. The major silicate perovskites are (Mg, Fe)SiO_3 (orthorhombic, bridgmanite) [2,3] and $CaSiO_3$ (high-pressure phase known as davemaoite) [4], which are likely the most abundant minerals on the Earth [5,6]. Plastic deformation in minerals of the lower mantle can lead to seismic anisotropy and can influence earthquake formation. Studying these mechanisms in perovskite as a function of pressure and temperature is therefore important for understanding the Earth's interior and deep geophysical processes [7].

The study of the mechanical properties and lattice defects of (Mg, Fe)SiO_3 perovskite under standard laboratory conditions is not feasible because this phase is unstable at ambient conditions and under the electron beam in TEM [8,9]. The extreme conditions in the lower mantle make experiments on these minerals highly challenging. An alternative way is to use analogue materials with similar crystallographic structures but different chemistry compositions, thereby simplifying experimental study. Insights from these analogues can be extrapolated to predict the response of the materials in the deep portion of the Earth. Typically, analogue materials have similar phase diagrams and cations charges but differ in their symmetries [10,11]. Substitutions at both cation sites are common; consequently, natural perovskites can deviate significantly from ideal stoichiometry [12]. This method has proven effective in elasticity studies. Additionally, it has been shown that materials with the same crystal structure and similar chemical bonding have similar mechanical response [13].

Perovskite has the ABX_3 structure with A and B cations having a variety of charges. The idealized perovskite structure is cubic (space group Pm3m) with a network of corner-linked BX_6 octahedra. The large A cations are located in the cavity formed by eight BX_6 octahedra. However, as the size of the A cation decreases, the B-X-B links have to bend to maintain contact between cations and anions. This is because the A cations become too small to remain in contact with the anions in the cubic structure. This tilting of BX_6 octahedra is determined by the A and B cation sizes, described by the tolerance factor, and reduces lattice symmetry at lower temperatures [14]. Most oxide perovskites are cubic

* Corresponding author.
E-mail address: mameyers@ucsd.edu (M.A. Meyers).

https://doi.org/10.1016/j.actamat.2025.121166
Received 7 April 2025; Received in revised form 13 May 2025; Accepted 20 May 2025
Available online 21 May 2025

at high temperatures but distorted to lower-symmetry forms such as orthorhombic (Pbnm) at lower temperatures due to atomic displacements. $CaTiO_3$ is isostructural with $MgSiO_3$, as both are $A^{2+}B^{4+}O_3$ perovskites and thus have the same space group at ambient conditions, transitioning from orthorhombic to tetragonal and to cubic as temperature rises [5,9]. They exhibit similar distortions because the SiO_6 and TiO_6 octahedra have similar rotation angles, indicating that $CaTiO_3$ is a structural analogue for $MgSiO_3$ for dislocation glide [11]. The lattice parameters of the $CaTiO_3$ orthorhombic structure (space group Pbnm) used in this study are a = 0.538 nm, b = 0.544 nm and c = 0. 7639 nm at ambient conditions (from Crystallography Open Database).

$CaTiO_3$ transitions from the orthorhombic to the tetragonal structure at around 1385 K and then to cubic at about 1520 K, resulting in changes in its creep properties. The temperature dependence of lattice parameters supports these phase transitions. Thus, $CaTiO_3$ can act as a useful analogue for exploring the high-temperature deformation mechanisms of silicate perovskite due to its structural similarities and phase transition behavior [9].

First-principles calculations predict that the $CaTiO_3$ Pbnm orthorhombic perovskite structure transforms to a post-perovskite Cmcm $CaIrO_3$ phase at 32.7 GPa, and then transitions to a post-post–perovskite structure at 71.7 GPa [15]. Guennou et al. [16] demonstrated that $CaTiO_3$ retains its Pbnm perovskite structure up to 60 GPa in diamond anvil cell experiments at room temperature. However, Truffet et al. [17] proposed that $CaTiO_3$ dissociates into CaO and $CaTi_2O_5$ at pressures above 60 GPa and temperatures up to 4500 K, rather than transforming into a post-perovskite phase.

Deep-focus earthquakes typically occur at depths of 300 to 700 km from the Earth's surface, where minerals are subjected to extreme pressures and temperatures. Phase transformations, shear, and defect propagation in minerals within subducted plates may be the causes of deep-focus earthquakes. This study is directed at better understanding the Earth's internal structure and behavior at these depths and deciphering the Earth's mantle dynamics with the shock waves involved in this process.

In summary, exploring $CaTiO_3$ within a pressure range suitable for experimental studies provides insights into ultra-high-pressure phenomena involved in planetary interiors, which are beyond the scope of experimental mineral physics. Thus, the main focus of the work presented herein is to generate, through high amplitude pulsed lasers and using a suitable simulant to (Mg, Fe)SiO_3 perovskite, a regime having similar pressure and temperature to the lower Earth mantle.

2. Experimental procedures

2.1. Laser shock compression and recovery

The Omega Laser Facility of Laboratory of Laser Energetics at University of Rochester was used to shock brittle $CaTiO_3$ under extreme loading conditions. Fig. 1 shows the sample, recovery capsule and tube filled with Aerogel; the setup is designed to decelerate and capture the shocked sample and recovery capsule. Prior to laser shock, a cylindrical single crystal $CaTiO_3$ target was encapsulated in a Cu cup by heating the latter and inserting the $CaTiO_3$ sample into it. They were allowed to cool down to minimize the gap between the sample and capsule, thus confining the $CaTiO_3$ cylinder. A 20 μm CH (polystyrene) ablator, 100 μm Cu foil, and Ø 3 × 5 mm $CaTiO_3$ cylinder single crystal sample were glued together by a thin layer of epoxy. Laser shock compression subjects materials to a unique regime with a duration of nanoseconds. The laser energy is deposited on CH (polystyrene) ablator, vaporizing it and producing a plasma. The pressure generated by this plasma launches a shock wave into the target. The use of impedance matched capsules is crucial for the successful recovery of the samples and their subsequent characterization. All results presented here come from one single laser shock experiment.

The strain rate is determined by the duration of a shock wave. Crack propagation is limited by the Rayleigh wave speed [18]. The ultrashort stress pulse duration (tens of nanoseconds including the shock release) is at least an order of magnitude smaller than the characteristic crack propagation time (microseconds) through the target. The impedance matched encapsulation ensures the sample's integrity by suppressing the full development of cracks, protecting it from catastrophic failure (e.g. fragmentation), thus enabling post shock characterization.

Copper was chosen as the encapsulation material due to its machinability and, more importantly, similar acoustic impedance (product of longitudinal sound speed and density) of 34.14 MPa·s/m,

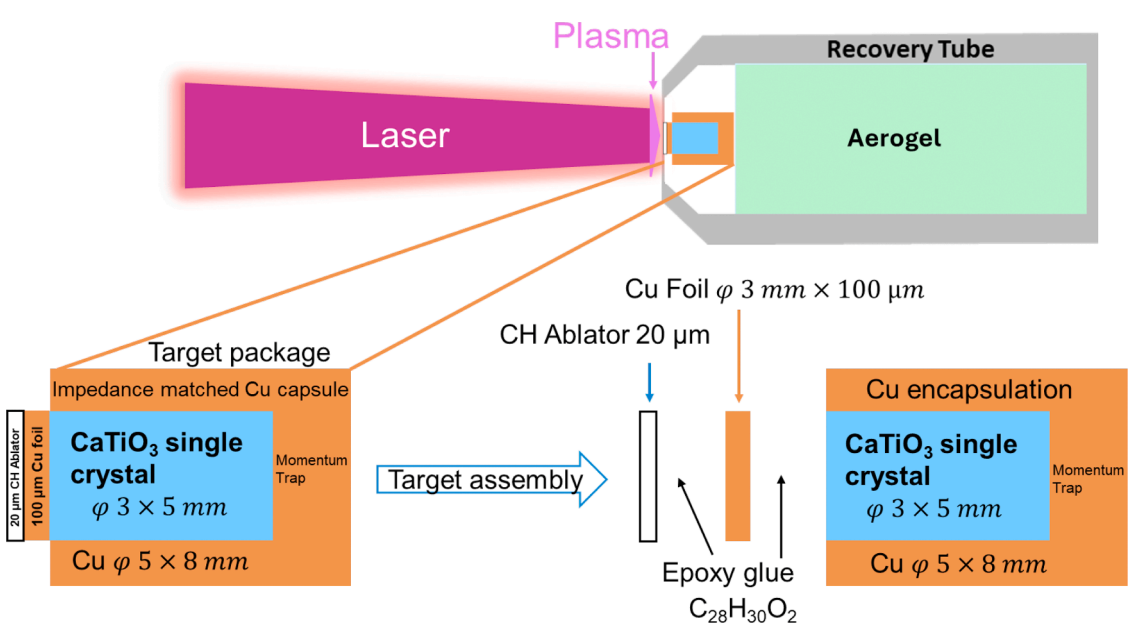

Fig. 1. Overall experimental setup for laser shock on [010] single crystal $CaTiO_3$ illustrating the target package that is mounted in a recovery tube. Single crystal $CaTiO_3$ cylinder is [010] oriented and has dimensions of ∅ 3 mm × 5 mm. Magnification of the target package, consisting of a 20 μm CH ablator (polystyrene) used to produce plasma under laser irradiation and a 100 μm Cu heat shield stuck in front of the $CaTiO_3$ sample, encapsulated in Cu cup and backed by momentum trap. The CH ablator, Cu foil, and $CaTiO_3$ sample were stuck together by epoxy glue.

compared to that of $CaTiO_3$, 35.79 MPa·s/m. Matching acoustic impedance can effectively minimize reflected tensile waves and maximize transmitted shock waves at interfaces/free surfaces. Using this method, brittle $CaTiO_3$ was recovered without excessive cracking. Shock compression establishes a uniaxial strain state which can be decomposed into hydrostatic (elastic) stress and deviatoric (plastic) stress. The high energy laser at Omega can reach the extreme stress of the Earth's interior (mantle pressures from 24 to 136 GPa), enabling probing the deformation mechanisms of geophysically relevant materials and conditions.

Using the laser shock technique, unprecedented states with extremely high pressures, temperatures, and strain rates can be experimentally achieved. The pressure generated by laser pulse is a function of laser parameters through the Lindl equation [19],

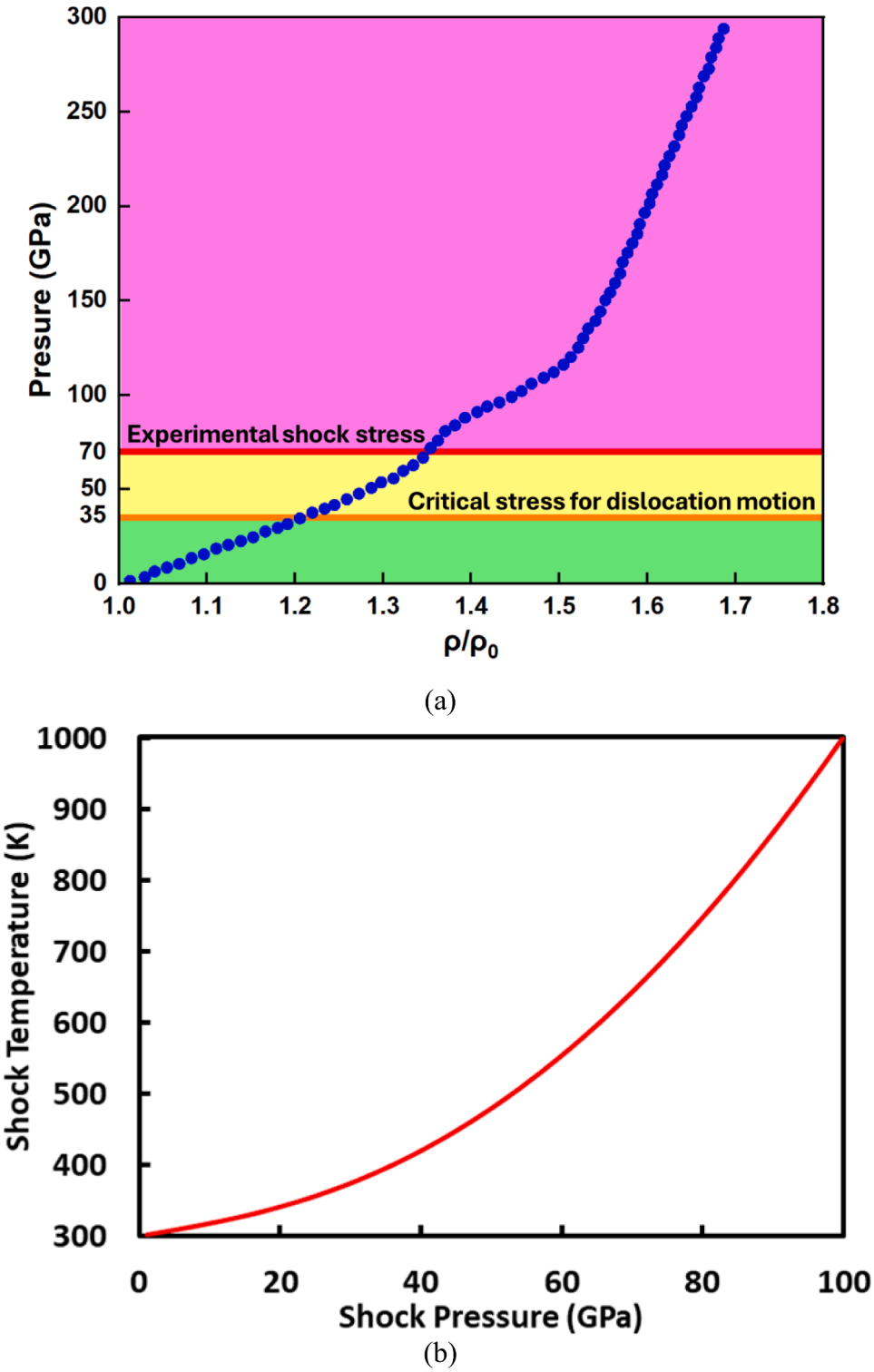

Fig. 2. (a) Shock Hugoniot curve Pressure vs relative density ρ/ρ_0 for $CaTiO_3$ [20,21]. The pressure used in the current experiment, 70 GPa, and the critical shock stress, 35 GPa, to initiate dislocation motion are marked in the plot. (b) Calculated shock temperature as a function of shock pressure for [010] $CaTiO_3$.

$$P(GPa) = (42 \pm 3) \cdot \left(\frac{I\left(\frac{TW}{cm^2}\right)}{\lambda\ (\mu m)} \right)^{0.71 \pm 0.01} \quad (1)$$

Where I=E/At is the laser intensity, E is the laser energy, A is the spot area, t is the laser duration, and λ is the laser wavelength, respectively. The sources are pulsed lasers of a 355 nm wavelength. The nominal laser energy for the experiment was 200.5 J, with a full width half max pulse duration of 1 nanosecond and square pulse shape. This value was estimated in other experiments conducted at Omega using VISAR. No VISAR was used in the current ride-along experiment. The laser spot size was 2.95 mm in diameter. Therefore, the estimated upper bound initial peak shock pressure in the $CaTiO_3$ sample was 70 GPa along the [010] direction.

2.2. Material source and characterization

Our single crystal $CaTiO_3$ perovskite cylinder was synthesized by SurfaceNet GmbH, with a diameter of 3 mm and a height of 5 mm. Copper capsule and foil were purchased and processed at the UCSD Campus Research Machine Shop. Focused ion beam (FIB) was used to prepare very thin foil specimens of about 100 nm for TEM. FEI Scios Dual Beam FIB/SEM was used with gallium ion beam for pattern/lamella milling at different voltages and currents. A thin Pt film of about 2 μm was deposited on the area of interest to protect the sample. TEM post-shock characterization was conducted by Thermofisher Talos 200X G2-S/TEM operating at 200 kV, enabling identification of the deformation and failure mechanisms at the nanometer scale. Both FIB and TEM were conducted at Nano3, UCSD. We did not grind or polish the surface of the post-shock sample to protect the areas directly subjected to laser shock. Thus, the defect structure was preserved in this preparation procedure.

3. Results and discussion

$CaTiO_3$ is a perovskite material with various applications in electronics, biomedical, and photocatalytic fields, yet our current understanding of its mechanical response under extreme pressures and strain rates is far from complete. There is only a dearth of observations of the microstructural mechanisms of shock compressed $CaTiO_3$ due to the difficulty of sample recovery [20]. Fig. 2 is the shock Hugoniot of $CaTiO_3$ up to 300 GPa [21]. The pressure P vs. relative density ρ/ρ_0 curve has an inflection at P~100 GPa. This is most probably due to a phase transition. Indeed, as mentioned above, there are reports of the orthorhombic to tetragonal and then to cubic transitions with increasing temperature. The pressure used in the current experiment, 70 GPa (marked in the plot), is below the threshold. The recovery technique used here enabled the capture of shocked $CaTiO_3$ with only minor cracks and therefore enabled characterization of the defect structure by TEM.

When a shock wave passes through a crystalline solid, it compresses it and usually induces plastic deformation due to shear stresses. In ductile crystalline solids, dislocation motion, twinning, and phase transformations are the predominant mechanisms to dissipate the imposed elastic energy. On the other hand, in brittle materials, defect mediated plasticity is often limited so that fracture becomes the dominant way to dissipate the imparted strain energy, resulting in catastrophic failure. Each deformation mechanism has a characteristic time scale and therefore is highly dependent on strain rate.

Laser shock generates a rapid uniaxial strain state with corresponding high hydrostatic pressure and shear stress components. The shear stresses directly result from the uniaxial strain condition; the lattice is compressed uniaxially along the shock propagation direction but cannot expand laterally due to the sufficiently larger lateral dimensions of the shocked region compared to the pulse length.

The generalized Hooke's Law has the form:

$$\varepsilon_{xx} = \frac{1}{E}\left[\sigma_{xx} - \nu\left(\sigma_{yy} + \sigma_{zz}\right)\right] \quad (2)$$

Shock compression subjects the material to uniaxial strain: $\varepsilon_{xx}=\varepsilon_{yy}=0$ and $\sigma_{xx}=\sigma_{yy}$. Thus:

$$\sigma_{xx} = \frac{\nu}{1-\nu}\sigma_{zz} \quad (3)$$

The amplitude of the deviatoric stresses τ_{max}, assuming elastic deformation during shock compression, is:

$$\tau_{max} = \frac{3}{4}(\sigma_{zz} - P) \quad (4)$$

σ_{zz} is the shock stress and P is the hydrostatic pressure. The latter is:

$$P = \frac{1}{3}\left(\sigma_{xx} + \sigma_{yy} + \sigma_{zz}\right) \quad (5)$$

Thus

$$P = \frac{\sigma_{zz}}{3}\left(\frac{1+\nu}{1-\nu}\right) \quad (6)$$

Therefore

$$\tau_{max} = \frac{\sigma_{zz}}{2}\left(\frac{1-2\nu}{1-\nu}\right) \quad (7)$$

Assuming a Poisson's ratio equal to 0.3 [22], one obtains, for elastic deformation:

$\tau_{max} = 20$ GPa at $\sigma_{zz} = 70$ GPa.

This is a very high value, and is a significant fraction of the shear modulus G of $CaTiO_3$ (101-107 GPa) [23–25].

The Peierls-Nabarro stress barrier (τ_{PN}) and dislocation energy are much higher in covalently and ionically bonded materials than in metals due to their high self-energy, leading to very high shear stresses required to move dislocations. Defects form on crystallographic planes with the maximum resolved shear stresses, reducing the local shear stresses and relaxing the stress state to nearly hydrostatic state. The shock induced temperature rise enhances defect mobility and thus lowers τ_{PN}, although it is still much higher than in metals, resulting in lower dislocation velocities [26]. Slip occurs on close-packed planes to minimize energy loss. The τ_{PN} of perovskite approaches its theoretical strength limit (0.1 G) [27], which is about 10 GPa. Hence, laser shock generates shear stresses (~20 GPa) that exceed the Peierls-Nabarro stress (~10 GPa) and dislocations are generated and can move. Since the Peierls-Nabarro stress τ_{PN} is the minimum shear stress that needs to be overcome for dislocations to move (10 GPa for perovskite), a critical shock stress of 35 GPa is required to enable the dislocation movements according to Eq. (7), as marked in Fig. 2(a).

For the temperature calculation, the literature was systematically scanned and all the necessary parameters as a function of pressure were obtained. Although there is considerable variation, the most reliable or average values were used. The parameters and predictions are given below.

$T_0 = 300$ K

Density ρ_0 was taken from the Materials Project.

$\rho_0 = 4.03$ g/cm^3

$V_0 = \frac{1}{\rho_0} = 0.25$ cm^3/g $= 0.25\times10^{-3}$ m^3/kg

Grüneisen parameter: there are different values provided in the literature. We used an average value and took values from [28,29]. The value used is:

$\gamma_0 = 1.86$

Heat capacity C_v: This was calculated from C_p using the equation in [30]:

$$C_p = C_v + \alpha^2 VKT \quad (8)$$

The calculated value is:

$C_v = 721$ J/(kg•K) = 98 J/(mol•K)

Pressure as a function of specific volume. This is obtained from an equation derived from the Rankine-Hugoniot conservation equations. The expression used is from [31]:

$$P = \frac{C_0^2(V_0 - V)}{[V_0 - S(V_0 - V)]^2} \tag{9}$$

$$U_s = C_0 + SU_p \tag{10}$$

$$U_p = \frac{U_s - C_0}{S} \tag{11}$$

Longitudinal sound velocity was taken from [23,32–34].

$C_0 = 8.88\times10^3$ m/s

S was taken from [34–36]. We used an average value.

S = 1.43

The shock temperature equation is a direct extension of the Rankine-Hugoniot conservation equations. It is given in, e. g., Meyers [31]. The temperature rise calculation is obtained from the Rankine-Hugoniot equation below.

$$T = T_0\exp\left[\left(\frac{\gamma_0}{V_0}\right)(V_0 - V)\right] + \frac{(V_0 - V)}{2C_v}P + \frac{\exp\left(-\frac{\gamma_0}{V_0}V\right)}{2C_v}\int_{V_0}^{V} P\cdot\exp\left(\frac{\gamma_0}{V_0}V\right)\left[2 - \left(\frac{\gamma_0}{V_0}\right)(V_0 - V)\right]dV \tag{12}$$

The predicted temperature rise as a function of pressure is provided in Fig. 2 (b). Shock temperature reaches about 642 K at 70 GPa. This is much below the melting temperature, 2250 K. Therefore, we are confident that these effects are not relevant to our results.

Hydrostatic pressure alone does not generate line defects in crystals; in contrast, shear stresses play an important role in plastic deformation and lattice defects formation such as dislocations, stacking faults, and twinning. Point defect concentration, however, can be affected by both hydrostatic and deviatoric stresses. Shear stresses play a significant role in phase transitions and, in some instances, may even dominate the process [37–39]. Driven by the high-amplitude stress pulse, these defects propagate inwards from the surface along specific crystallographic orientations. They intersect and generate additional defects and plastic work. Shear-induced plasticity induces localized heating which in turn produces localized thermal softening and reduces the mechanical barrier for further plastic deformation. There is substantial evidence that shear promotes structural changes. Bridgman [37,40] first proposed that a shear stress superimposed on hydrostatic pressure lowers the threshold for structural phase transitions and accelerates their kinetics. Teller [38] and Enikolopian [41] indicated that shear strains significantly influence the reaction kinetics. Levitas [42] also reviewed the crucial role that shear plays in promoting phase transformations.

The conventional, bright-field and dark-field TEM, and HRTEM images in Fig. 3 provide a baseline comparison of unshocked $CaTiO_3$ with a sample subjected to laser shock compression at 70 GPa. The unshocked sample exhibits a very low density of defects and anti-phase boundaries. The significant differences observed between the two samples confirm that the shock-induced features are not artifacts introduced during FIB preparation.

As illustrated in Fig. 4, the shock direction is along [010]. The dislocations are aligned parallel to the [110] and [$\bar{1}$10] directions, while the slip plane is identified as (001) in the FIB-prepared sample. The subsequent figures (Figs. 5–10) detail the shock-induced defects.

Two-beam bright-field and dark-field images (Fig. 5) reveal a significantly higher density of defects in the 70 GPa shocked sample compared to the unshocked one (Fig. 3). Perpendicular dislocations and antiphase domain boundaries, and shear band-like features are heavily entangled and intertwined.

Weak-beam dark-field TEM image (Fig. 6) shows dislocations oriented at a 45° angle to the shock direction. The density of these dislocations decreases with distance from the shock surface, eventually disappearing at a certain depth. This gradient is consistent with the decay of the shock wave as it propagates away from the laser energy deposition surface. The dislocations are arranged in the (001) planes,

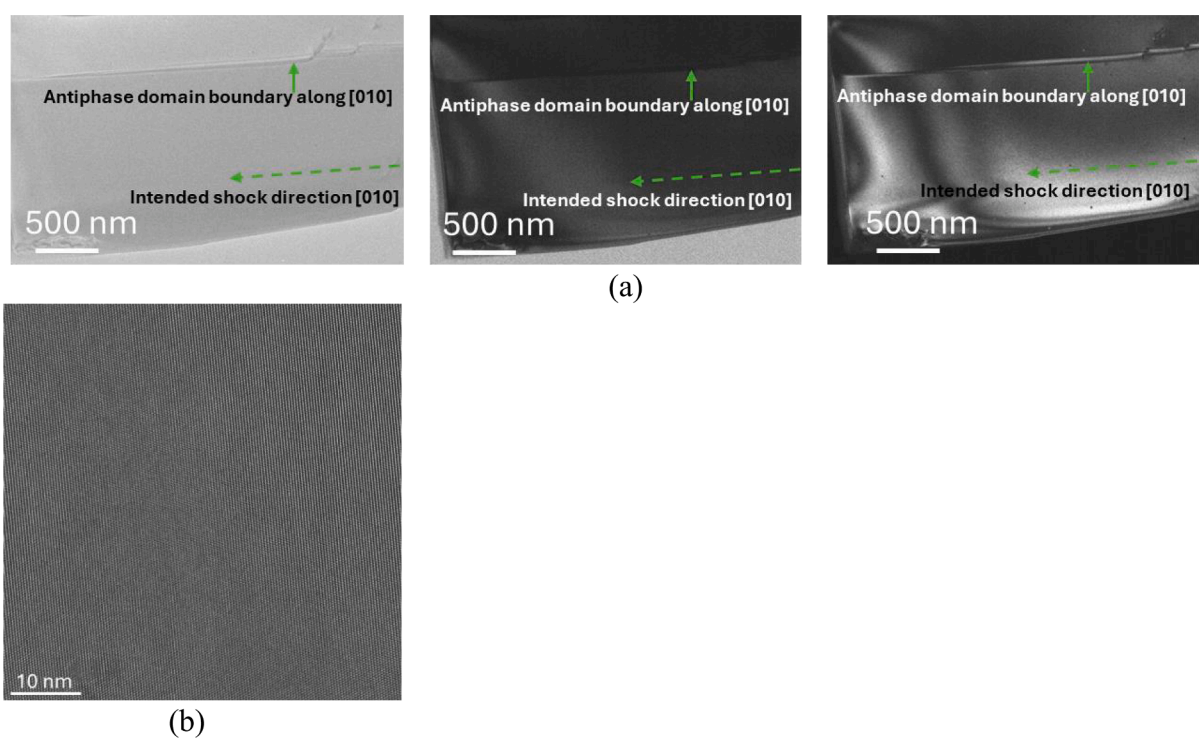

Fig. 3. (a) Conventional, bright-field, and dark-field low magnification TEM images of unshocked $CaTiO_3$. It has a very low density of defects and antiphase boundaries. (b) HRTEM image of the unshocked $CaTiO_3$.

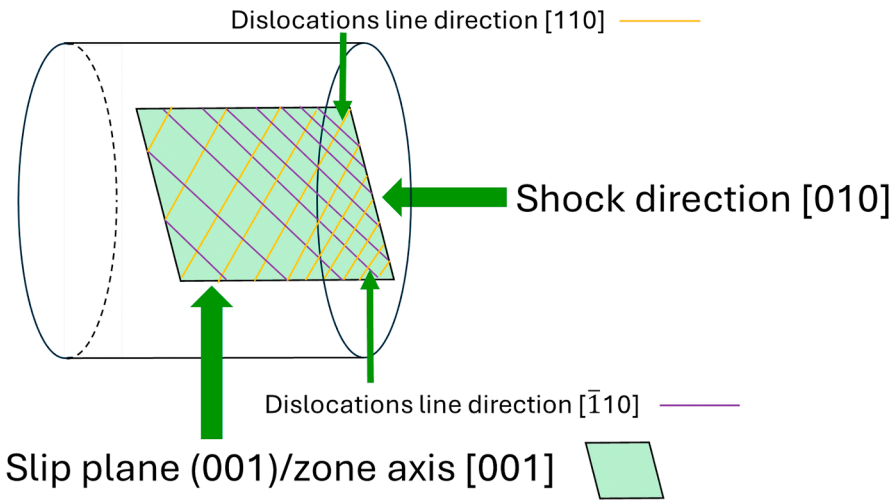

Fig. 4. Illustration of the FIB sample prepared for TEM (not to scale). The shock direction is [010]. The dislocation lines are parallel along [110] and [$\bar{1}$10] directions and the slip plane is (001).

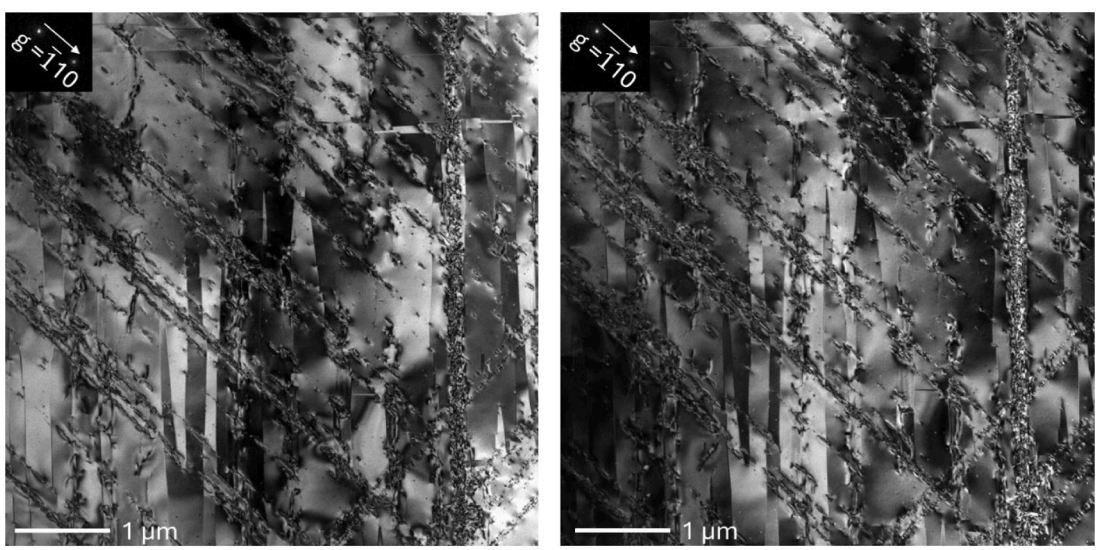

Fig. 5. Two-beam condition (a) bright-field and (b) dark-field TEM images. Significantly more defects such as dislocations, antiphase domain boundaries, and shear band-like morphology are observed in the sample shocked at 70 GPa compared to the unshocked one.

with spacings ranging from approximately 20 nm to 350 nm.

The dislocation density is shown in Fig. 7 down to 12 μm depth below the shock surface; a general decreasing trend from $\sim 15\times10^{12}$ to $\sim 2\times10^{12}$ m^{-2} is observed. This dislocation density in the laser shocked $CaTiO_3$ sample is very high, close to that of the highly deformed metals (above the order of 10^{12} m^{-2}). The interactions between these defects are expected to occur under laser shock compression, resulting in high defect densities and localized effects, including the loss of atomic order, shear band formation, and plastic heating. The low-magnification conventional, bright- and dark-field TEM images (Fig. 8) show that the laser-shocked region has dislocations and antiphase boundaries (APBs) along [010] and [100] under the [010] shock direction. Two sets of dislocations appear to be crystallographically aligned along mutually perpendicular [110] and [$\bar{1}$10] directions on (001) planes, respectively. Isolated domain boundaries have widths of tens to hundreds of nanometers. Antiphase domains exhibiting similar morphology were observed by Wang and Liebermann in natural perovskite crystals [5]. Fig. 9 illustrates the main slip system in the crystal unit cell of $CaTiO_3$, which shows the [110] and [$\bar{1}$10] dislocation lines on the (001) slip plane.

In Fig. 10, nanobeam electron diffraction and fast-Fourier transform (FFT) patterns in some regions exhibit extra spots which might result from double diffraction. There is another possible explanation for this phenomenon. The stacking nature of alternating neutral CaO and TiO_2 planes is regarded as the characteristic of perovskites [43]. However, the vulnerability to laser for CaO and TiO_2 planes might be different. Under laser shock compression, the complicated physical/chemical reactions might deplete or extract either CaO or TiO_2 planes so that the resulting layer defects might lead to the appearance of the extra spots in electron diffraction patterns. Nevertheless, whether this forms a second phase needs more investigation.

We present below the results of several studies; many other slip systems are observed at different temperatures. The perovskite structure generally has dislocations with <110> or <100> Burgers vectors; <110> dislocations can be found both at room temperature and high temperatures whereas <100> dislocations are found predominantly at high temperatures [44]. Besson et al. [9] demonstrated using TEM that all the dislocations observed in deformed single crystal $CaTiO_3$ were of

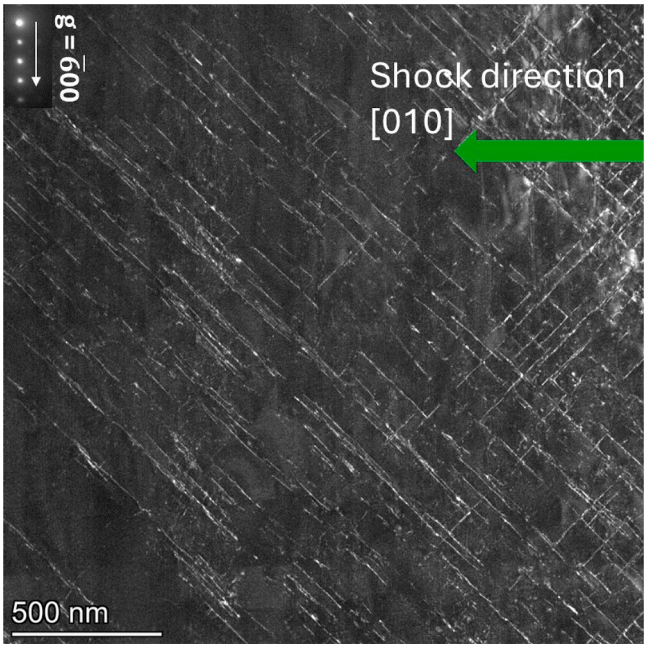

Fig. 6. Weak-beam dark-field condition TEM image. Dislocations [110] and [$\bar{1}$10] are 45° from the shock direction [010] down to 2 μm depth below the shock surface. Dislocation density generally decreases from the surface and eventually disappears at certain depth.

screw type. Poirier et al. [45] found that creep is controlled by dislocation gliding at high stresses and low temperatures. Mecklenburgh et al. [46] observed slip systems [110](001) and [$\bar{1}$10](001) through torsion and compression experiments on $(Ca_{0.9}Sr_{0.1})TiO_3$ perovskite at temperatures between 1350 and 1550 K. Wang et al. [5] found that the heat treated and deformed natural perovskite crystal $CaFe^{3+}_{0.1}Nb^{5+}_{0.1}Ti^{4+}_{0.8}O_3$ exhibits the slip systems [110](001) and [$\bar{1}$10](001), similar to our observations. Besson et al. [9,47] discovered that [100] natural single crystal $CaTiO_3$ specimens compressed along the [100] direction favor the [001](110) slip system, and specimens compressed along the [1$\bar{1}$0] direction favor the [100](010) slip system under creep tests at temperatures up to 1973 K. Doukhan and Doukhan [8] found that the easy glide systems of $CaTiO_3$ are [$\bar{1}$11](12$\bar{1}$) by micro scratches at room temperature; although the corresponding Burgers vector <111> is not the shortest lattice translation, dislocation gliding on these systems can prevent bringing various cations too close to each other during dislocation glide.

Orthorhombic $CaTiO_3$ exhibits significantly higher normalized Peierls-Nabarro stress than cubic $SrTiO_3$, which demonstrates orthorhombic distortions. All dislocations undergo lattice friction; however, glide occurs more easily on [$\bar{1}$10](001). While [100](010) and [010](100) are the easiest slip systems in cubic perovskite, they are accompanied by [110](001) easy glide system in orthorhombic $CaTiO_3$. Lattice friction increases as orthorhombic distortions increase [11]. In $CaTiO_3$, significant lattice friction is expected for any orientation of dislocation lines. Another notable effect of orthorhombic distortion is the presence of domains that persist at high temperatures and pressures. These domain boundaries can serve as obstacles to dislocation motion, similar tograin boundaries. The opposite, dislocations pinning the domain boundaries, is also a possible interaction. This is because the domains can more esily than dislocations [48]. Phase transitions may give rise to APBs. These domain boundaries prefer to align with low indices planes parallel to {001} planes of minimum surface energy [8]. In contrast, very few APBs are present in the low-temperature samples as evidenced in our unshocked sample. Dislocations are common in minerals subjected to high stress, relatively high strain rate, and moderate temperature. In the shocked $CaTiO_3$ sample, [010] and [100] antiphase domains, which are rarely observed in the unshocked material, become dominant. This domain structure change is attributed to a structural phase transition in perovskite at temperatures below 1585 K. Dislocations are dominant in the material and often interact with these domain

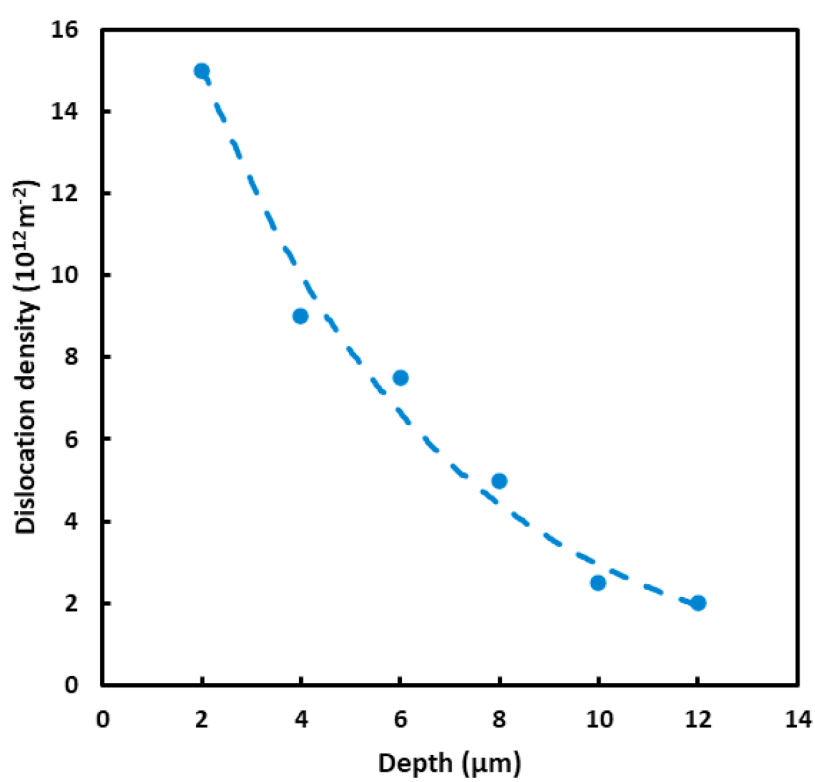

Fig. 7. Dislocation densities in shocked $CaTiO_3$. Distance up to 12 μm depth below the shock surface, showing a decreasing trend from ~15×10^{12} to ~2×10^{12} m^{-2}.

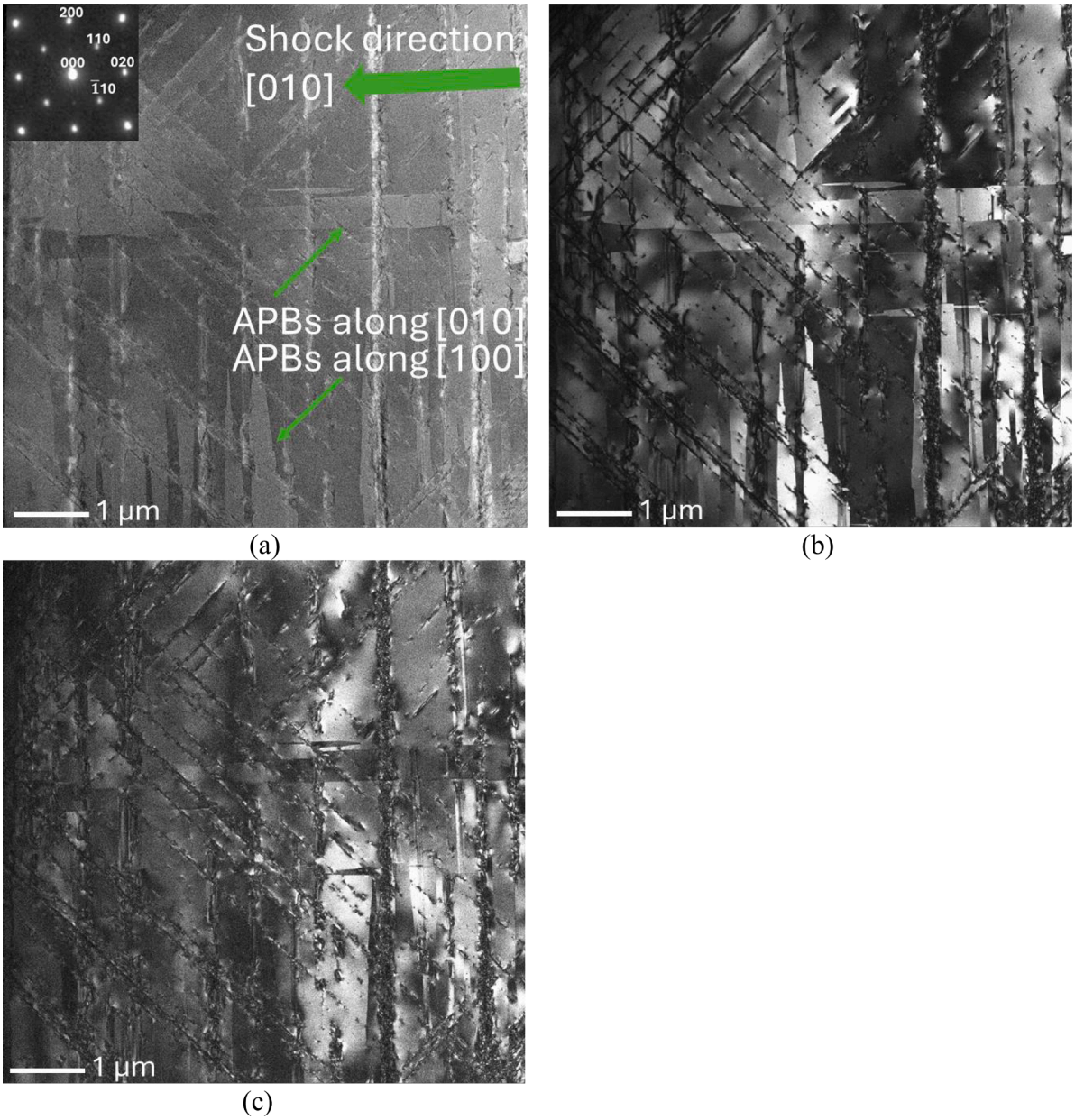

Fig. 8. (a) Antiphase domain boundaries are along [010] and [100] directions with corresponding SAED; (b) and (c) are its bright- and dark-field images showing the defect features. Dislocations are generally along mutually perpendicular [110] and [$\bar{1}$10] directions on (001) planes. Isolated domain boundaries have widths of tens to hundreds of nanometers.

boundaries [5].

Under quasi-static loading, heat can be dissipated quickly to the surrounding without causing a temperature rise. In contrast, shock loading reduces material's volume, generating substantial work which is dissipated as heat and inducing a temperature rise at the shock front. Elevated temperatures significantly increase defect mobility by lowering the energy barrier for plastic deformation, generating localized thermal softening and further facilitating this process [49]. If the temperature at the shock front exceeds the melting point of $CaTiO_3$ (2250 K), melting may occur; as a result, the material is unable to sustain shear stress.

Since $CaTiO_3$ has a positive Clapeyron slope [17] and a relatively higher atomic packing factor (0.58) than our previously studied materials (Si, Ge, SiC, B_4C, and olivine [27]) which have lower atomic packing factors (0.14 - 0.4), amorphization as the deformation mechanism under extreme loading conditions is not favored. $CaTiO_3$ behaves more like metals, responding to deformation mainly by dislocation motion rather than these covalently-bonded materials which amorphize under shock compression. This in turn confirms our previous conjecture.

This process is significant in planetary sciences as it may contribute to deep-focus earthquakes by generating stress waves. It is also relevant to meteorite impacts due to the role of shock waves.

4. Conclusions

$CaTiO_3$ was used as an analogue material for studying (Mg, Fe)SiO_3 and $CaSiO_3$ which are the most abundant minerals in the Earth mantle. Laser shock was applied to a [010] oriented orthorhombic single crystal $CaTiO_3$, subjecting it to a uniaxial strain state at a pressure of 70 GPa, characteristic of the Earth mantle. The corresponding maximum shear stress was ~20 GPa. This is significantly higher than the threshold for dislocation motion, the Peierls-Nabarro stress τ_{PN} (10 GPa for $CaTiO_3$). Materials with covalent and ionic bonding, such as $CaTiO_3$, are

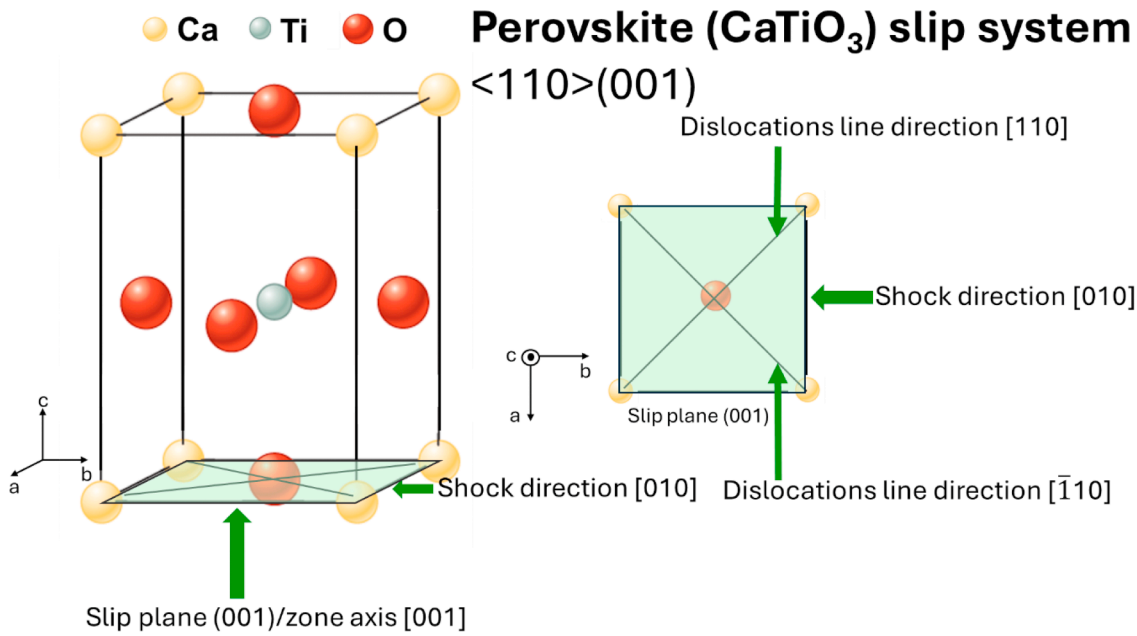

Fig. 9. Slip system in crystal unit cell of $CaTiO_3$, showing the [110] and [$\bar{1}$10] dislocation lines on the (001) slip plane under the [010] shock direction.

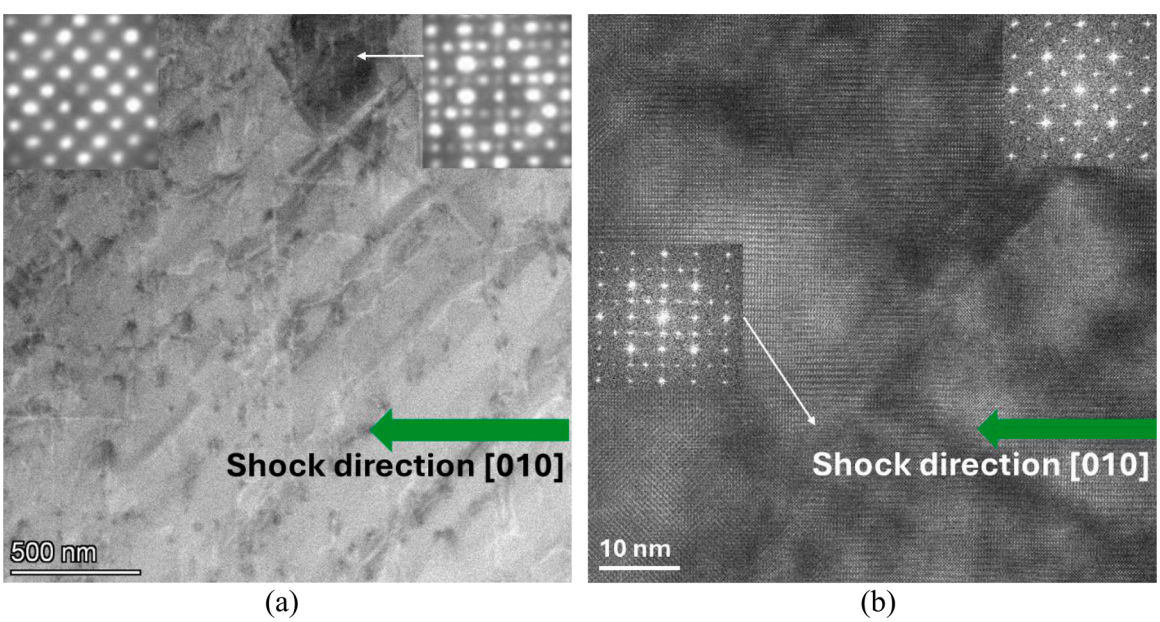

Fig. 10. Extra diffraction spots in some regions of shocked $CaTiO_3$ confirmed by (a) nanobeam diffraction pattern and (b) FFT.

characterized by high Peierls-Nabarro stress (τ_{PN}), which increases resistance to dislocation motion. The high τ_{PN} of $CaTiO_3$ makes plastic deformation more difficult, resulting in the accumulation of higher deviatoric stresses within the material. The shock temperature was calculated from the Rankine- Hugoniot conservation equations and parameters obtained in the literature. For the 70 GPa pressure, the temperature reached 642 K, which is much lower than the melting point (2250 K).

The laser shock generated a high density of defects in $CaTiO_3$. Most defects are mutually perpendicular dislocations. The dominant slip systems in our study are [110](001) and [$\bar{1}$10](001). The density of antiphase domain boundaries increased substantially after laser shock, along [010] and [100] directions. Dislocation density ranged from 15×10^{12} m^{-2} at the shock surface to 2×10^{12} m^{-2} at 12 μm from the shocked surface.

Because of its positive Clapeyron slope and higher atomic packing factor, $CaTiO_3$ behaves more like metals, deforming mainly by dislocation motion in contrast with covalently-bonded materials that respond by amorphization under shock compression; this confirms our previous conjecture.

This profuse dislocation generation holds significance in planetary science, as it may provide insights into the mechanisms underlying deep-focus earthquakes and the effects of meteorite impacts.

CRediT authorship contribution statement

Boya Li: Writing – original draft, Methodology, Investigation, Formal analysis, Data curation, Conceptualization. **Shiteng Zhao:** Writing – review & editing, Project administration, Methodology, Conceptualization. **Marc A. Meyers:** Writing – review & editing,

Supervision, Resources, Project administration, Investigation, Conceptualization.

Declaration of competing interest

The authors declare that they have no known competing financial interests or personal relationships that could have appeared to influence the work reported in this paper.

Acknowledgements

We thank Dr. Camelia Stan at Lawrence Livermore National Laboratory and the staff of the Laboratory for Laser Energetics for performing the laser shock experiments. Ping Che Lee at UCSD, Nano3 staff Dr. Jeff Wu and Dr. Zhicheng Long at UCSD, and Dr. Mingjie Xu at UCI, are gratefully acknowledged for providing guidance with the FIB and TEM. This research was partially supported by the Department of Energy, National Nuclear Security Administration under award DE-NA0004147. Boya Li appreciatively acknowledges fellowships from the Program of Materials Science and Engineering, UCSD.

References

[1] F.V. Kaminsky, Carbonatitic lower-mantle mineral association, in. Springer Geology, Springer, 2017, pp. 205–228, https://doi.org/10.1007/978-3-319-55684-0_6.
[2] T. Sharp, Bridgmanite-named at last: the most abundant mineral in Earth's interior gets a name, Science 346 (1979) (2014) 1057–1058, https://doi.org/10.1126/science.1261887.
[3] O. Tschauner, C. Ma, J.R. Beckett, C. Prescher, V.B. Prakapenka, G.R. Rossman, Discovery of bridgmanite, the most abundant mineral in Earth, in a shocked meteorite, Science 346 (2014) 1100–1102.
[4] O. Tschauner, S. Huang, S. Yang, M. Humayun, W. Liu, S.N. Gilbert Corder, H. A. Bechtel, J. Tischler, G.R. Rossman, Discovery of davemaoite, $CaSiO_3$-perovskite, as a mineral from the lower mantle, Science 374 (1979) (2021) 891–894. https://www.science.org.
[5] Y. Wang, R.C. Liebermann, Electron microscopy study of domain structure due to phase transitions in natural perovskite, Phys. Chem. Miner. 20 (1993) 147–158.
[6] S.A.T. Redfern, High-temperature structural phase transitions in perovskite, J. Phys. Condens. Matter 8 (1996) 8267–8275.
[7] S. Couper, S. Speziale, H. Marquardt, H.P. Liermann, L. Miyagi, Does heterogeneous strain act as a control on seismic anisotropy in Earth's lower mantle? Front. Earth Sci. 8 (2020) 540449 https://doi.org/10.3389/feart.2020.540449.
[8] N. Doukhan, J.C. Doukhan, Dislocations in Perovskites $BaTiO_3$ and $CaTiO_3$, Phys. Chem. Miner. 13 (1986) 403–410.
[9] P. Besson, J.P. Poirier, G.D. Price, Dislocations in $CaTiO_3$ perovskite deformed at high-temperature: a transmission electron microscopy study, Phys. Chem. Miner. 23 (1996) 337–344.
[10] J.A. Souza, J.P. Rino, A molecular dynamics study of structural and dynamical correlations of $CaTiO_3$, Acta Mater. 59 (2011) 1409–1423, https://doi.org/10.1016/j.actamat.2010.11.003.
[11] D. Ferré, P. Carrez, P. Cordier, Peierls dislocation modelling in perovskite ($CaTiO_3$): comparison with tausonite ($SrTiO_3$) and $MgSiO_3$ perovskite, Phys. Chem. Miner. 36 (2009) 233–239, https://doi.org/10.1007/s00269-008-0272-0.
[12] K. Wright, G.D. Price, J.P. Poirier, High-temperature creep of the perovskites $CaTiO_3$ and $NaNbO_3$, Phys. Earth Planet. Inter. 74 (1992) 9–22.
[13] P. Li, S.I. Karato, Z. Wang, High-temperature creep in fine-grained polycrystalline $CaTiO_3$, an analogue material of (Mg, Fe)SiO_3 perovskite, Phys. Earth Planet. Inter. 95 (1996) 19–36.
[14] M.R. Levy, Chapter 3: perovskite perfect lattice. Crystal Structure and Defect Property Predictions in Ceramic Materials, Department of Materials, Imperial College London, 2005, pp. 79–114.
[15] C. Xu, B. Xu, Y. Yang, H. Dong, A.R. Oganov, S. Wang, W. Duan, B. Gu, L. Bellaiche, Prediction of a stable post-post-perovskite structure from first principles, Phys. Rev. B Condens. Matter Mater. Phys. 91 (2015) 020101, https://doi.org/10.1103/PhysRevB.91.020101.
[16] M. Guennou, P. Bouvier, B. Krikler, J. Kreisel, R. Haumont, G. Garbarino, High-pressure investigation of $CaTiO_3$ up to 60 GPa using x-ray diffraction and Raman spectroscopy, Phys. Rev. B Condens. Matter Mater. Phys. 82 (2010) 134101, https://doi.org/10.1103/PhysRevB.82.134101.
[17] B. Truffet, G. Fiquet, G. Morard, M.A. Baron, F. Miozzi, M. Harmand, A. Ravasio, M. Mezouar, F. Guyot, High pressure dissociation of $CaTiO_3$ perovskite into CaO and $CaTi_2O_5$, Phys. Earth Planet. Inter. 334 (2023) 106968, https://doi.org/10.1016/j.pepi.2022.106968.
[18] L.B. Freund, Crack propagation in an elastic solid subjected to general loading–II. Non-uniform rate of extension, J. Mech. Phys. Solids 20 (1972) 141–152.
[19] J. Lindl, Development of the indirect-drive approach to inertial confinement fusion and the target physics basis for ignition and gain, Phys. Plasmas 2 (1995) 3933–4024, https://doi.org/10.1063/1.871025.
[20] W.J. Nellis, Systematics of compression of hard materials, J. Phys. Conf. Ser. (2008) 062005, https://doi.org/10.1088/1742-6596/121/6/062005.
[21] R.F. Trunin, G.V. Simakov, M.A. Podurets, B.N. Moiseyev, L.V. Popov, Dynamic compressibility of quartz and quartzite at high pressure, Izv. Acad. Sci. USSR Phys. Solid Earth 1 (1971) 13–20.
[22] A. Boudali, A. Abada, M. Driss Khodja, B. Amrani, K. Amara, F. Driss Khodja, A. Elias, Calculation of structural, elastic, electronic, and thermal properties of orthorhombic $CaTiO_3$, Phys. B Condens. Matter 405 (2010) 3879–3884, https://doi.org/10.1016/j.physb.2010.06.020.
[23] Y.D. Sinelnikov, G. Chen, R.C. Liebermann, Elasticity of $CaTiO_3$ $\pm CaSiO_3$ perovskites, Phys. Chem. Miner. 25 (1998) 515–521.
[24] G.J. Fischer, Z. Wang, S.I. Karato, Elasticity of $CaTiO_3$, $SrTiO_3$ and $BaTiO_3$ perovskites up to 3.0 GPa: the effect of crystallographic structure, Phys. Chem. Miner. 20 (1993) 97–103.
[25] S. Tariq, A. Ahmed, S. Saad, S. Tariq, Structural, electronic and elastic properties of the cubic $CaTiO_3$ under pressure: a DFT study, AIP Adv. 5 (2015), https://doi.org/10.1063/1.4926437.
[26] K. Katagiri, T. Pikuz, L. Fang, B. Albertazzi, S. Egashira, Y. Inubushi, G. Kamimura, R. Kodama, M. Koenig, B. Kozioziemski, G. Masaoka, K. Miyanishi, H. Nakamura, M. Ota, G. Rigon, Y. Sakawa, T. Sano, F. Schoofs, Z.J. Smith, K. Sueda, T. Togashi, T. Vinci, Y. Wang, M. Yabashi, T. Yabuuchi, L.E. Dresselhaus-Marais, N. Ozaki, Transonic dislocation propagation in diamond, Science 382 (2023) 69–72. https://www.science.org.
[27] S. Zhao, B. Li, B.A. Remington, C.E. Wehrenberg, H.S. Park, E.N. Hahn, M. A. Meyers, Directional amorphization of covalently-bonded solids: A generalized deformation mechanism in extreme loading, Mater. Today 49 (2021) 59–67, https://doi.org/10.1016/j.mattod.2021.04.017.
[28] A.M. Hofmeister, H.K. Mao, Pressure derivatives of shear and bulk moduli from the thermal Grüneisen parameter and volume-pressure data, Geochim. Cosmochim. Acta 67 (2003) 1215–1235, https://doi.org/10.1016/S0016-7037(02)01289-9.
[29] K.S. Knight, Structural and thermoelastic properties of $CaTiO_3$ perovskite between 7 K and 400 K, J. Alloys Compd. 509 (2011) 6337–6345, https://doi.org/10.1016/j.jallcom.2011.03.014.
[30] P. Gillet, F. Guyot, G.D. Price, B. Tournerie, A. Le Cleach, Phase changes and thermodynamic properties of $CaTiO_3$. Spectroscopic data, vibrational modelling and some insights on the properties of $MgSiO_3$ perovskite, Phys. Chem. Miner. 20 (1993) 15–170.
[31] M.A. Meyers, Dynamic Behavior of Materials, John Wiley & Sons, 1994.
[32] S. Webb, I. Jackson, J.F. Gerald, Viscoelasticity of the titanate perovskites $CaTiO_3$ and $SrTiO_3$ at high temperature, Phys. Earth Planet. Inter. 115 (1999) 259–291. www.elsevier.comrlocaterpepi.
[33] R. Placeres-Jiménez, L.G.V. Gonçalves, J.P. Rino, B. Fraygola, W.J. Nascimento, J. A. Eiras, Low-temperature elastic anomalies in $CaTiO_3$: dynamical characterization, J. Phys. Condens. Matter 24 (2012), https://doi.org/10.1088/0953-8984/24/47/475401.
[34] R.C. Liebermann, L.E.A. Jones, A.E. Ringwood, Elasticity of aluminate, titanate, stannate and germanate compounds with the perovskite structure, Phys. Earth Planet. Inter. 14 (1977) 165–178.
[35] T.J. Ahrens, M.L. Johnson, Shock wave data for minerals, in: Mineral Physics and Crystallography, A Handbook of Physical Constants, 2, American Geophysical Union, 1995, pp. 143–184.
[36] S.S. Batsanov, Shock and Materials, Springer, 2018.
[37] P.W. Bridgman, Effects of high shearing stress combined with high hydrostatic pressure, Phys. Rev. 48 (1935) 825.
[38] E. Teller, On the speed of reactions at high pressures, J. Chem. Phys. 36 (1962) 901–903, https://doi.org/10.1063/1.1732687.
[39] H.C. Chen, J.C. Lasalvia, V.F. Nesterenko, M.A. Meyers, Shear localization and chemical reaction in high-strain, high-strain-rate deformation of Ti–Si powder mixtures, 46 (1998) 3033–3046.
[40] P.W. Bridgman, Shearing phenomena at high pressures, particularly in inorganic compounds, Proceed. Am. Academy Arts Sci. 71 (1937) 387–460.
[41] N.S. Enikolopian, Some aspects of chemistry and physics of plastic flow, Pure Appl. Chem. 57 (1985), 1707–171.
[42] V.I. Levitas, Phase transformations, fracture, and other structural changes in inelastic materials, Int. J. Plast. 140 (2021) 102914, https://doi.org/10.1016/j.ijplas.2020.102914.
[43] D. Yu, J. Zhang, F. Wang, M. Zhao, K. Du, S. Shu, J. Zou, Y. Wang, High-symmetry epitaxial growth under solvothermal conditions: a strategy for architectural growth of tubular and nontubular $CaTiO_3$ microstructures with regular geometrical morphologies and tunable dimensions, Cryst. Growth Des. 13 (2013) 3138–3143, https://doi.org/10.1021/cg400514q.
[44] J.P. Poirier, S. Beauchesne, F. Guyot, Deformation mechanisms of crystals with perovskite structure, in: Perovskite: A Structure of Great Interest to Geophysics and Materials Science, 45, Wiley, 1989, pp. 119–123.
[45] J.P. Poirier, Creep of Crystals: High-Temperature Deformation Processes in Metals, Ceramics and Minerals, Cambridge University Press, 1985.
[46] J. Mecklenburgh, F. Heidelbach, E. Mariani, S. Mackwell, F. Seifert, Rheology and microstructure of $(Ca_{0.9},Sr_{0.1})TiO_3$ perovskite deformed in compression and torsion, J. Geophys. Res. Solid Earth 115 (2010), https://doi.org/10.1029/2009JB006520.

[47] M. Hu, H.R. Wenk, D. Sinitsyna, Microstructures in natural perovskites, Am. Mineral. 77 (1992) 359–373. https://pubs.geoscienceworld.org/msa/ammin/article-pdf/77/3-4/359/4217963/am77_359.pdf.
[48] O. Preuß, E. Bruder, W. Lu, F. Zhuo, C. Minnert, J. Zhang, J. Rödel, X. Fang, Dislocation toughening in single-crystal $KNbO_3$, J. Am. Ceramic Soc. 106 (7) (2023) 4371–4381.
[49] S. Zhao, B. Kad, E. Hahn, L. Chen, Y. Opachi, K. More, B. Remington, C. Wehrenberg, J. Lasalvia, W. Yang, H. Quan, M. Meyers, Shock-induced amorphization in covalently bonded solids, Proceed. EPJ Web Conf., EDP Sci. 03027 (2018), https://doi.org/10.1051/epjconf/201818303027.